

Vano Lett. Author manuscript; available in PMC 2012 February 9.

Published in final edited form as:

Nano Lett. 2011 February 9; 11(2): 498–504. doi:10.1021/nl103315t.

Optical Sizing of Immunolabel Clusters through Multispectral Plasmon Coupling Microscopy

Hongyun Wang, Guoxin Rong, Bo Yan, Linglu Yang, and Björn M. Reinhard*
Department of Chemistry and The Photonics Center, Boston University, Boston, Massachusetts 02215

Abstract

The wavelength dependent scattering cross-sections of self-assembled silver nanoparticle clusters of known size (n) were measured on five different wavelength channels between 427 and 510 nm through correlation of multispectral imaging and scanning electron microscopy. A multivariate statistical analysis of the spectral response of this training set provided a correlation between spectral response and cluster size and enabled a classification of new measurements into four distinct nanoparticle association levels (I1 – I4) whose compositions were dominated by monomers (I1), dimers (I2), trimers and tetramers (I3), and larger clusters (I4), respectively. One potential application of the optical sizing approach is to map association levels of silver immunolabels on cellular surfaces. We demonstrate the feasibility of this approach using silver immunolabels targeted at the epidermal growth factor receptor on A431 cells in a proof of principle experiment. The ability to measure immunolabel association levels on sub-cellular length scales in an optical microscope provides new opportunities for experimentally assessing receptor density distributions on living cells in solution.

Keywords

epidermal growth factor receptor; receptor clustering; silver nanoparticles; nanoplasmonics

Introduction

Some receptors such as the epidermal growth factor receptor (EGFR)¹ require synergistic interactions between individual receptors to produce a successful signaling event in response to an external stimulus.2⁻11 Consequently, the signaling efficiency has been indicated to depend on the receptor's local concentration and spatial distribution.12⁻15 To investigate the potential role of the spatial receptor organization for controlling the EGFR signaling activity in detail, it is necessary to map the EGFR near- and long-range order in the plasma membrane, ideally of living cells. Snapshots of the receptor distribution on isolated membranes at defined times with nanometer spatial resolution have traditionally been obtained using antibody functionalized gold nanoparticles in transmission electron microscopy (TEM) immunolabeling.14[,] 16[,] 17 TEM studies are, however, not applicable to investigate receptor clustering on living cells and require a special membrane preparation. Optical microscopy is a desirable alternative for characterizing receptor distributions on living cells in solution, but a direct mapping of the EGFR density with high spatial

^{*}Corresponding author. bmr@bu.edu.

resolution in the light microscope is challenged by the diffraction limit of light of ~400 nm in the visible. Much shorter distances of up to ~10 nm can be measured optically by quantifying the fluorescence resonance energy transfer (FRET) between donor and acceptor dye molecules;18 homo-FRET imaging of green fluorescence protein (GFP) tagged EGFRs was successfully applied to determine the average EGFR association levels in pixels of approx. $300 \times 300 \text{ nm}^2$. This study revealed that even in the absence of ligand, the cell surface EGFRs are already predimerized or in an oligomerized state. The "optical sizing" in this work did, however, not allow a further distinction of clusters with more than three EGFRs and could not address the spatial organization of the observed EGFR oligomers on length scales of tens of nanometers. To close the gap between the spatial FRET barrier of ~10 nm and the diffraction limited resolution of the confocal microscope, and to obtain more detailed information about the organization of EGFRs and EGFR oligomers on length scales of tens of nanometers, Abulrob et al. used near-field scanning microscopy (NSOM) to image fluorescent antibody labeled EGFR in the plasma membrane of HeLa cells.²⁰ Abulrob et al. found that EGFRs are associated into clusters with an average diameter of 150 nm before and after exposure to EGF. Sophisticated microscopies such as NSOM are not necessarily available in standard biophysical or biochemical laboratories. In addition, NSOM, like all other fluorescence based nanoscopies²¹, suffers from the limited photostabilities of organic dye labels which are prone to bleaching and blinking. These instabilities make long continuous observations or the monitoring of individual molecules with high temporal resolution difficult. Noble metal nanoparticles are potential alternatives for fluorescence dyes as labels of cell surface receptors. The optical properties of gold and silver nanoparticles are determined by coherent collective oscillations of the conduction band electrons, the so called plasmons.²² Gold and silver nanoparticles with diameters > 20 nm are very efficient light scatterers at their resonance frequency and generate strong optical signals free of blinking or bleaching. ²³, ²⁴ Individual nanoparticles can be detected in light microscopy, provided that the background excitation can be eliminated through darkfield²⁵ or total internal reflection illumination²⁶. When two particles approach each other to within ~one particle diameter, the particle plasmons couple and the resulting plasmon hybridization²⁷ leads to a spectral shift that is detectable in the far-field.^{28–34} The distance dependent spectral response of coupled nanoparticles provides additional functionality in sensing and imaging and has been utilized, for instance, for monitoring EGFR association during endocytosis, 35 the detection of EGFR overexpression, 36, 37 the imaging of caspase-3 activation38 or the nuclear uptake of peptides39, and the monitoring of sub-diffraction limit distances between individual, laterally diffusing cell surface species 40, 41. Although the applications of plasmon coupling in imaging have been very diverse, most of the work performed thus far used plasmon coupling either to enhance the signal from individual nanoparticle labels upon clustering or to detect changes in nanoparticle clustering as result of a particular biochemical process of interest. In this work, we do not aim to measure changes in plasmon coupling, but instead seek to achieve an optical sizing of twodimensional nanoparticle clusters without the need for monitoring their formation. The ability to simultaneously localize and size nanoparticle clusters in an optical microscope (instead of an electron microscope) provides new opportunities for investigating many-body interactions using plasmon coupling microscopy in biophysics and material science. In this manuscript we implement and characterize an optical sizing approach for nanoparticle clusters and demonstrate the applicability of this approach for mapping the association levels of silver immunolabels, which are targeted at EGFR, on living cells in a proof of principle experiment.

Results and Discussion

Multispectral Plasmon Coupling Microscopy and Multivariate Spectral Analysis

Our approach for an optical sizing of two-dimensional nanoparticle clusters involved in a first step a systematic characterization of the spectral response of clusters of known size (n) using multivariate analysis strategies⁴². The spectral discriminators identified in this process were then to be applied to characterize the spectral response of clusters of unknown size in a second step. The nanoparticle clusters of known size required for the first step of our experimental approach were fabricated using a template assisted self-assembly process (Figure 1a) of HS-(CH₂)₁₁-(OCH₂CH₂)₆-OCH₂-COOH functionalized silver nanoparticles with an average diameter of 30 ± 4 nm on glass (see Methods in Supporting Information).43 ⁴⁴ The cluster binding sites in these arrays were written with a cluster edge-to-edge separation of $\Lambda = 7$ µm to avoid any interactions between the individual clusters. The size distribution of the fabricated clusters could be shifted in a rational fashion through variation of the diameter (D) of the e-beam generated binding sites.⁴³ Figure 1b shows SEM images of representative silver nanoparticle clusters of different sizes and their corresponding scattering spectra. Going from n = 1 to n = 7, the peak wavelength of the randomly chosen clusters red-shifts by ~100 nm, and the spectral width (full width at half maximum) increases from 59 nm to 103 nm. The global size dependence of the spectral response in Figure 1b confirms that the cluster scattering spectra contain valuable information about nanoparticle cluster sizes. The spectral differences between some clusters are, however, subtle. For instance, the spectra of n = 2.3 have similar peak wavelengths and can only be differentiated through the broader width of the n = 3 spectrum. One important task of this manuscript will therefore be to establish the precision with which different nanoparticle association levels can be differentiated. Some of the anticipated applications of the optical sizing method include the simultaneous analysis of many nanoparticle clusters distributed across an entire cell, ideally, with high temporal resolution. A spatially resolved spectral analysis of an entire cell surface using a spectrometer requires a confocal scanning which limits the temporal resolution. We therefore decided to use a multispectral imaging approach, instead, which provides spectral information of the entire field of view within a few images.

We have recently introduced a plasmon coupling microscopy which uses ratiometric imaging on two color channels in a widefield darkfield microscope to monitor for spectral shifts in nanoparticle assemblies laterally diffusing on a cell surface.40, 41, 45 An optical sizing of nanoparticle clusters requires more detailed spectral information than the detection of spectral shifts and necessitates an expansion of the number of monitored wavelength channels. We therefore implemented a multispectral plasmon coupling microscopy using a fast filter switching device (Till Oligochrome) that enables a rapid (6 ms) interchange between five different excitation filters (F1 = 427 ± 5 nm; F2 = 445 ± 10 nm; F3 = 473 ± 5 nm; $F4 = 494 \pm 10$ nm; $F5 = 510 \pm 5$ nm, all filters had transmission efficiencies of > 90%) for an illumination at multiple wavelengths. The nanofabricated clusters were imaged in an inverted microscope (Olympus IX71) under darkfield illumination through a high numerical aperture (N.A.) oil darkfield condenser (N.A. 1.2-1.4). The scattered light was collected using a $60 \times$ oil immersion objective (NA = 0.65) and captured on an electron multiplying CCD (EMCCD) detector (Andor Ixon+). At the chosen magnification the effective pixel size was 350 nm \times 350 nm. Using this detector and the filter switching device we were able to record a full set of 5 images in approximately 40 ms, resulting in a peak temporal resolution for monitoring the entire field of view (~2000 µm²) of approximately 25 Hz. The data presented in this work were recorded with frame rates of 2 Hz.

The recorded monochromatic images (128×128 pixels) were background-subtracted and corrected for the spectral profile of the excitation light by dividing through the normalized

scattering intensities from an ideal whitelight scatterer recorded under the different excitation conditions. The integrated intensities for each cluster on the different wavelength channels (F1–F5) were normalized by dividing through the peak intensity of the brightest channel. After imaging in the darkfield microscope, the cluster arrays were transferred into the scanning electron microscope (SEM) to determine the sizes (n) of the individual clusters. Control experiments in which the samples were SEM inspected before and after optical characterization verified that n did not change in the course of the experiments.

In the next step we characterized the spectral response of the fabricated clusters with known n through discriminant function analysis (DFA)⁴⁶, 47(see Methods in Supporting Information). DFA is a rigorous mathematical procedure that identifies linear combinations of variables in a data set comprising several groups so that the first discriminant function (DF1) accounts for the largest part of the variation between the groups, the second discriminant function (DF2) accounts for the largest fraction of the remaining variation and so forth. The DFs span a DF space in which different groups - in our case nanoparticle clusters of different size (n) - separate most strongly. DFA is similar to principal component analysis (PCA)⁴⁸, but different from PCA, the membership of a measurement to a specific group is known in DFA and used to separate the groups.

Figure 2a contains a scatter plot of 266 clusters of different sizes in the DF1-DF2 plane and a contour plot of the fitted cluster size data. The cluster size surface was fitted using a ridge estimator implemented in the gridfit⁴⁹ program. The members of the individual cluster sizes are somewhat spread in the DF1-DF2 plane, which is attributed to the fact that the applied optical sizing approach averages over different cluster configurations for a given n. Variations in the cluster geometry and interparticle separation influence the cluster spectra and limit the accuracy of the optical sizing. Despite the spread of the experimental data, the contour plot shows some important general trends. The average cluster size increases with decreasing DF1 and at low DF1 the average cluster size also increases with increasing DF2. The contour plot confirms that larger cluster sizes localize in different areas of the DF1-DF2 plane than smaller clusters and monomers. To illustrate the trends in the cluster size distribution more clearly, we have subdivided the fitted DF1–DF2 plane into 4 areas (I1–I4) corresponding to cluster size contour intervals of n(I1) = [1-1.8,] (blue), n(I2) = [1.8-3.2](turquoise), n(I3) = [3.2-4.1] (yellow), and n(I4) > 4.1 (brown) in Figure 2b. The average cluster sizes (\bar{n}) for the individual areas are as follows: $\bar{n}(I1) = 1.1 \pm 0.3$; $\bar{n}(I2) = 2.3 \pm 0.7$; \bar{n} (I3) = 3.7 ± 1.0; \bar{n} (I4) = 4.5 ± 1.0.

Figure 2b also contains pie charts of the composition of the different areas I1–I4. The compositions of I1 and I2 are dominated by monomers and dimers, respectively. In fact, 90 % of all monomers lie in I1 and 78% of all dimers lie in I2. As the number of structural degrees of freedom increases with growing cluster size, it becomes more difficult to differentiate between different cluster sizes. Consequently, I3 and I4 have more complex compositions but they still exhibit systematic differences. 79% of all clusters in I3 have sizes of $n \le 4$, whereas 50% of all clusters in I4 have sizes of n > 4. 54% of all trimers and 46% of all tetramers are located in I3, whereas 70% of all pentamers and 83% of all hexamers are located in I4. These numbers indicate a gradual transition from mid-sized clusters ($n \le 4$) in I3 to larger (n > 4) clusters in I4.

Validation of Optical Sizing through Multispectral Plasmon Coupling Microscopy

To further test the ability of the optical sizing approach to determine the association levels of cluster of unknown size, we performed an independent validation experiment. We recorded the multispectral response of a total of 200 random nanoparticle clusters and assigned them to I1–I4 based on their coordinates in the DF1–DF2 space derived with the training set. After their optical characterization we determined the real size of the clusters using the

SEM, which enabled us to correlate the optically derived association levels I1–I4 with the actual sizes of the clusters. The result of these studies is shown in Figure 3. Similar as in Figure 2b the pie charts represent the composition the individual association levels. A comparison of the pie charts in Figures 2b and Figure 3 shows that the individual association levels I1–I4 in the two independent experiments have nearly identical compositions. The similarity is further corroborated by the average cluster sizes (\bar{n}) for I1–I4: \bar{n} (I1) = 1.2 ± 0.5; \bar{n} (I2) = 2.4 ± 0.8; \bar{n} (I3) = 3.7 ± 1.0; \bar{n} (I4) = 4.7 ± 1.0. These values are almost identical to the ones obtained before with the training set.

Although the assignment of each individual cluster based on its position in the DF1–DF2 plane is subject to some error, which increases with cluster size, the optical sizing approach achieves a partitioning of the training set into four unique nanoparticle association levels as defined by I1 – I4. These association levels provide the means for a quantitative - and as the validation experiments now confirm - reproducible description of two-dimensional nanoparticle clustering. The new optical cluster sizing modality makes it possible to compare relative aggregation states in different cluster ensembles using conventional light microscopy.

EGFR Immunolabels for Plasmon Coupling Microscopy

Live-cell imaging experiments are typically performed in imaging buffers, such as Hank's buffer (137.93 mM NaCl, 5.33 mM KCl, 4.13 mM NaHCO₃, 0.441 mM KH₂PO₄, 0.338 mM Na₂HPO₄, 1.35 mM MgSO₄, 1.26 mM CaCl₂, 5.56 mM D-glucose, supplemented with 10 mM HEPES pH 7.4), in which unprotected gold and silver nanoparticles tend to agglomerate. We used in this work silver nanoparticles with an average diameter of 30±4 nm. To avoid an agglomeration of the particles in buffer solution, we first stabilized the particles through assembly of a monolayer of short polyethylene glycols (HS-(CH₂)₁₁-(OCH₂CH₂)₆-OCH₂-COOH) on the particle surface. In a subsequent step we then covalently functionalized the nanoparticles with an anti-EGFR antibody. ⁵⁰ A detailed description of the particle preparation is provided in the Methods section of the Supporting Information. We chose 30 nm silver nanoparticles as labels in this study because silver nanoparticles are more sensitive probes in PCM than gold nanoparticles. 40 Silver nanoparticles have larger scattering cross-sections than gold nanoparticles of equal size and previous calibration studies^{28, 31} have shown that the spectral shift of the resonance wavelength (λ_{res}) as function of decreasing interparticle separation (s) is larger for silver than for gold nanoparticle dimers. In addition, we find that under our experimental conditions, the silver resonance is blue-shifted with regard to the peak scattering intensity of the A431 cells on glass investigated in this work (see Figure S1).

To test the stability of the anti-EGFR functionalized silver nanoparticles, the particles were resuspended in Hank's buffer to a total concentration of 1.2×10^{11} particles/mL and then incubated with A431 cells for 10 mins under the same conditions used in our imaging experiments. The particles were then recovered and analyzed through UV-Vis spectroscopy and dynamic light scattering. In Figure 4a we plot the UV-Vis spectra of the nanoparticles before and after incubation with the cells. Both samples have the same peak resonance wavelength and no systematic shift is observed between the spectra. Similarly, the size distribution as obtained by dynamic light scattering (DLS) superimpose (Figure 4b) further confirming the stability of the applied nanoparticle labels under live cell imaging conditions. The stability of the nanoparticle labels in solution justifies the assumption that nanoparticle association is restricted to the cell surface.

Mapping Nanoparticle Association Levels on A431 cells

Having in hand a method that enables to convert multispectral responses emitted from nanoparticle clusters at random positions in the field of view into effective cluster sizes, we next set out to apply this method to determine local association levels of EGFR targeted immunolabels on cellular surfaces. The focus of this study was to map the immunolabel distribution on the cell surface before endocytosis related mechanism lead to the formation of three-dimensional nanoparticle clusters in endosomes.³⁵ Consequently, we chose the experimental conditions as to minimize the uptake of nanoparticle labeled EGFR through endocytosis. The cells (60% confluence) were synchronized in the G0 phase of the cell cycle by serum-starvation overnight. The cells were subsequently incubated with Hank's buffer containing 0.1% Tween 20 for two hours at 4°C and subsequently washed with copious amounts of ice-cold Hank's buffer. The cells were then incubated with a solution of 1.2×10¹¹ particles/mL of anti-EGFR functionalized 30 nm diameter silver nanoparticles in Hank's buffer for 10 mins at 4°C. In the last step the cells were washed with Hank's buffer, transferred to the optical microscope and imaged immediately. Figure 5 shows a representative darkfield image of cells labeled with anti-EGFR functionalized silver nanoparticles. Especially in the peripheral region of the cell surface nanoparticle labels are clearly recognizable as vivid blue or blue-green spots.

The silver nanoparticle clusters of the DF training set were assembled on polylysine functionalized glass. Glass has a refractive index (n_r) of around 1.46, and the refractive index of lipid bilayers lies in the range of $n_r=1.46\pm0.06.\ ^{51}$ The refractive index at the glass/buffer interface is hence comparable to that at the interface between cellular plasma membrane and surrounding buffer. The DF1–DF2 plane derived from nanofabricated clusters of defined sizes is therefore also an appropriate reference system to characterize the association levels of EGFR targeted nanoparticles on cellular surfaces. We focus in the following on an optical nanoparticle cluster sizing in flat peripheral cell regions where - as can be seen in Figure 5 - the nanoparticle labels can be imaged with very good signal-to-noise. Recent studies have indicated a peripheral enhancement of EGF induced signaling, 52 which underlines the importance of these areas for EGFR signaling.

In panels a1-a3 of Figure 6, we show darkfield images of silver nanoparticle labeled cell membrane sections from three different cells (1-3). The images were recorded under whitelight illumination using the EMCCD detector. Panels b1-b3 of Figures 6 show composite images of the same membrane regions that were constructed from the individual monochromatic images recorded on the monitored wavelength channels (F1-F5). The color of the individual pixels in these images reflect the relative intensities of the 510 and 494 nm (red), 473 and 445 nm (green), and 427 nm (blue) wavelength channels. The red, green, and blue intensities in each pixel were normalized by dividing through a constant scaling factor for each composite image (highest pixel intensity in all original monochromatic images). The observation of a wide dynamic color range in the labeled cell membrane areas in panels b1-b3 of Figure 6 is already indicative of different association levels of the silver nanoparticles on the cell surface for the chose experimental conditions. The optical cluster sizing approach, which we calibrated with silver nanoparticle clusters of known size, enables a more quantitative description of the average nanoparticle association levels as function of location on the cell surface. To that end we corrected the original five monochromatic images for the cellular background and the excitation light profile and normalized each pixel "spectrum" by dividing through the value of the highest intensity channel. For all pixels with a total intensity above the average cellular background we calculated the corresponding coordinates in the plane spanned by DF1 and DF2. The latter are defined linear combinations of the relative intensities on the monitored wavelength channels whose definitions are given in the Supporting Information. Each pixel was then assigned to one of the nanoparticle association levels I1-I4 based on its location in the DF1-

DF2 plane (Figure 2b). This processing converted the original five monochromatic images of each cell into one spatial map of the local nanoparticle association levels I1–I4. The resulting maps for the three investigated membranes are shown in panels c1–c3 of Figure 6.

We find that for all three cells the immunolabels are significantly clustered on the cell membrane; the contribution from individual nanoparticles to the integrated cluster size distribution is very low as is illustrated by the pie charts included in Figures 6c1–3. We point out that individual nanoparticles have lower scattering cross-sections than clusters. Consequently, we cannot exclude that the optical response from a particular region on the cell membrane will be dominated by the nanoparticle cluster distribution in this area, even if it contains individual nanoparticles as well. A potential underestimation of the contribution from individual, dispersed immunolabels in cell regions that contain clusters does, however, not question the method's ability to detect immunolabel clustering and to map relative nanoparticle association levels across the membrane.

Assuming that the local immunolabel density is proportional to the EGFR density, nanoparticle association level maps provide insight into relative receptor densities as function of location. It is therefore instructive to analyze the spatial distribution of the nanoparticle association into monomers (I1), dimers (I2), medium (I3) and large clusters (I4) on the cell surface in more detail. For cells 1 and 2 in panels c1 and c2 of Figure 6, we find that the nanoparticle association levels are lower at the cell edge on the right than in areas closer to the cell center on the left. Especially for cell 1 in Figure 6c1, the dimers (I2, turquoise) are preferentially located at the edge of the membrane. Cell 2 in Figure 6c2 exhibits higher dimer contributions at the membrane edge on the right, but dimer areas can also be found interspersed with areas whose optical response is dominated by trimers and tetramers (I3, yellow) and mid-sized to large clusters (I4, brown) in the central part of the membrane section. On the left the contribution from larger clusters (I4) becomes dominant as observed for cell 1.

While cells 1&2 show similar trends for the spatial nanoparticle association level distributions, the map for cell 3 in Figure 6c3 is qualitatively different. One obvious difference is that for cell 3 large areas of the membrane are void of nanoparticle labels. Those areas that contain immunolabels show, however, very high degrees of nanoparticle clustering. A direct comparison of the relative contributions from I1–I4 using the pie charts provided in Figure 6 reveals that the contribution from large clusters (I4) is highest and the contribution from nanoparticle dimers (I2) lowest for cell 3. We conclude that for cell 3 confinement of the immunolabels to special membrane regions is accompanied by - on average - higher association levels than for the other two investigated cells.

In this work we focus primarily on the development and validation of the multispectral plasmon coupling imaging approach for optical cluster sizing. The above analysis verifies, however, that this approach is also applicable to map the average association levels of anti-EGFR silver immunolabels on cellular sufaces. The demonstrated ability to resolve differences in the local association levels of silver nanoparticles on cell membranes motivates further systematic studies to characterize the spatial EGFR distribution under physiological conditions using a larger set of cells, improved immunolabels with optimized binding affinities, and gentle cell preparation strategies.

Conclusions

We have shown that multispectral plasmon coupling microscopy in combination with a multivariate statistical data analysis enables to distinguish individual silver nanoparticles from nanoparticle clusters of different association levels. We could characterize silver

nanoparticles and their clusters by assigning them to one of four association level based on their multispectral response: I1 (94% monomers), I2 (72% dimers), I3 (79% trimers and tetramers), I4 (50% pentamers and hexamers). We have used this optical sizing modality to map the association levels of silver immunolabels targeted at the epidermal growth factor receptor (EGFR) as function of their location on A431 cells. Since immunolabeling densities are correlated with receptor densities, the resulting nanoparticle association maps can provide valuable insight into the spatial organization of the receptor density. The EGFR density is a cancer biomarker and imaging methods that enable its quantification on subcellular levels in a simple optical set-up could have significant impact on current cancer diagnostics and staging modalities. The developed optical nanoparticle cluster sizing approach is compatible with live cell imaging conditions and is also of interest for fundamental research, for instance, for studying the dynamics of receptor distributions as response to external stimuli in real time.

Supplementary Material

Refer to Web version on PubMed Central for supplementary material.

Acknowledgments

This work was financially supported by the National Institutes of Health through grant 5R01CA138509-02.

REFERENCES

- 1. Schlessinger J. Cell. 2000; 103(2):211–225. [PubMed: 11057895]
- 2. Gadella TWJ, Jovin TM. Journal of Cell Biology. 1995; 129(6):1543-1558. [PubMed: 7790353]
- 3. Martin-Fernandez M, Clarke DT, Tobin MJ, Jones SV, Jones GR. Biophysical Journal. 2002; 82(5): 2415–2427. [PubMed: 11964230]
- Ichinose J, Murata M, Yanagida T, Sako Y. Biochemical and Biophysical Research Communications. 2004; 324(3):1143–1149. [PubMed: 15485674]
- 5. Sako Y, Minoghchi S, Yanagida T. Nature Cell Biology. 2000; 2(3):168–172.
- Kawashima N, Nakayama K, Itoh K, Itoh T, Ishikawa M, Biju V. Chemistry A European Journal. 2010; 16:1186–1192.
- 7. Saffarian S, Li Y, Elson EL, Pike LJ. Biophysical Journal. 2007; 93(3):1021–1031. [PubMed: 17496034]
- 8. Clayton AHA, Orchard SG, Nice EC, Posner RG, Burgess AW. Growth Factors. 2008; 26(6):316–324. [PubMed: 18937111]
- Clayton AHA, Walker F, Orchard SG, Henderson C, Fuchs D, Rothacker J, Nice EC, Burgess AW. Journal of Biological Chemistry. 2005; 280(34):30392–30399. [PubMed: 15994331]
- Clayton AHA, Tavarnesi ML, Johns TG. Biochemistry. 2007; 46(15):4589–4597. [PubMed: 17381163]
- Gan HK, Walker F, Burgess AW, Rigopoulos A, Scott AM, Johns TG. The Journal of Biological Chemistry. 2007; 282(5):2840–2850. [PubMed: 17092939]
- Mayawala K, Vlachos DG, Edwards JS. FEBS Letters. 2005; 579:3043–3047. [PubMed: 15896781]
- 13. Hsieh M-Y, Yang S, Raymond-Stinz MA, Steinberg S, Vlachos DG, Shu W, Wilson B, Edwards JS. IET Systems Biology. 2008; 2:256–272. [PubMed: 19045821]
- 14. Ariotti N, Liang H, Xu Y, Zhang Y, Yonekubo Y, Inder K, Du G, Parton RG, Hancock JF, Plowman SJ. Molecular and Cellular Biology. 2010; 30(15):3795–3804. [PubMed: 20516214]
- 15. Whitty A. Nature Chemical Biology. 2008; 4:435–439.
- Yang S, Raymond-Stintz MA, Ying W, Zhang J, Lidke DS, Steinberg SL, Williams L, Oliver JM, Wilson BS. Journal of Cell Science. 2007; 120(16):2763–2773. [PubMed: 17652160]

17. van Belzen N, Rijken PJ, Hage WJ, De Laat SW, Verkleij AJ. Journal of Cellular Physiology. 1988; 134:413–420. [PubMed: 3258312]

- Lakowicz, JR. Principles of Fluorescence Spectroscopy. Vol. Vol. 2. New York: Kluwer Academic; 1999.
- Bader AN, Hofman EG, Voortman J, van Bergen en Henegouwden PMP, Gerritsen HC. Biophysical Journal. 2009; 97:2613–2622. [PubMed: 19883605]
- 20. Abulrob A, Lu Z, Baumann E, Vobornik D, Taylor R, Stanimirovic D, Johnston LJ. The Journal of Biological Chemistry. 2010; 285:3145–3156. [PubMed: 19959837]
- 21. Hell SW. Science. 2007; 316(5828):1153-1158. [PubMed: 17525330]
- 22. Kreibig, U.; Vollmer, M. Optical Properties of Metal Clusters. Berlin: Springer; 1995.
- 23. Yguerabide J, Yguerabide EE. Analytical Biochemistry. 1998; 262(2):157–176. [PubMed: 9750129]
- 24. Yguerabide J, Yguerabide EE. Analytical Biochemistry. 1998; 262(2):137–156. [PubMed: 9750128]
- 25. Schultz S, Smith DR, Mock JJ, Schultz DA. Proceedings of the National Academy of Sciences. 2000; 97(3):996–1001.
- Sonnichsen C, Geier S, Hecker NE, von Plessen G, Feldmann J, Ditlbacher H, Lamprecht B, Krenn JR, Aussenegg FR, Chan VZH, Spatz JP, Moller M. Applied Physics Letters. 2000; 77(19):2949–2951.
- 27. Prodan E, Radloff C, Halas NJ, Nordlander P. Science. 2003; 302(5644):419–422. [PubMed: 14564001]
- Reinhard BM, Siu M, Agarwal H, Alivisatos AP, Liphardt J. Nano Letters. 2005; 5(11):2246– 2252. [PubMed: 16277462]
- 29. Su KH, Wei QH, Zhang X, Mock JJ, Smith DR, Schultz S. Nano Letters. 2003; 3(8):1087-1090.
- 30. Rechberger W, Hohenau A, Leitner A, Krenn JR, Lamprecht B, Aussenegg FR. Optics Communications. 2003; 220(1–3):137–141.
- 31. Yang L, Wang H, Reinhard BM. The Journal of Physical Chemistry C. 2010; 114:4901–4908.
- 32. Jain PK, Huang WY, El-Sayed MA. Nano Letters. 2007; 7(7):2080-2088.
- 33. Funston AM, Novo C, Davis TJ, Mulvaney P. Nano Letters. 2009; 9(4):1651–1658. [PubMed: 19271775]
- 34. Elghanian R, Storhoff JJ, Mucic RC, Letsinger RL, Mirkin CA. Science. 1997; 277(5329):1078–1081. [PubMed: 9262471]
- 35. Aaron J, Travis K, Harrison N, Sokolov K. Nano Letters. 2009; 9:3612–3618. [PubMed: 19645464]
- Aaron J, Nitin N, Travis K, Kumar S, Collier T, Park SY, Jose-Yacaman M, Coghlan L, Follen M, Richards-Kortum R, Sokolov K. Journal of Biomedical Optics. 2007; 12:034007. [PubMed: 17614715]
- 37. Crow MJ, Grant G, Provenzale JM, Wax A. American Journal of Roentgenology. 2009; 192:1021–1028. [PubMed: 19304709]
- 38. Jun Y-W, Sheikholeslami S, Hostetter DR, Tajon C, Craik CS, Alivisatos AP. Proceedings of the National Academy of Sciences. 2009; 42:17735–17740.
- 39. Qian W, Huang X, Kang B, El-Sayed MA. Journal of Biomedical Optics. 2010; 15(4):046025. [PubMed: 20799827]
- 40. Rong G, Wang H, Reinhard BM. Nano Letters. 2010; 10:230-238. [PubMed: 20017502]
- 41. Rong G, Wang H, Skewis LR, Reinhard BM. Nano Letters. 2008; 8:3386–3393. [PubMed: 18788826]
- 42. Sharma, S. Applied Multivariate Techniques. New York: John Wiley and Sons; 1996.
- 43. Yan B, Thubagere A, Premasiri R, Ziegler L, Dal Negro L, Reinhard BM. ACS Nano. 2009; 3:1190–1202. [PubMed: 19354266]
- 44. Yang L, Yan B, Premasiri RW, Ziegler LD, Dal Negro L, Reinhard BM. Advanced Functional Materials. 2010; 20(16):2619–2628.
- 45. Wang H, Reinhard BM. The Journal of Physical Chemistry C. 2009; 113:11215–11222.

46. MacFie HJH, Gutteridge CS, Norris JR. Journal of General Microbiology. 1978; 104:67–74. [PubMed: 624936]

- 47. Windig W, Haverkamp J, Kistemaker PG. Analytical Chemistry. 1983; 55(1):81-88.
- 48. Jolliffe, IT. Principal Component Analysis. 2 ed.. Berlin: Springer; 2002.
- 49. D'Errico, J. Surface Fitting Using Gridfit. Matlab Central. Natick, MA: The Mathworks, Inc.; [Accessed Sep. 18, 2010]. http://www.mathworks.de/matlabcentral/fileexchange/8998-surface-fitting-using-gridfit
- Skewis LR, Reinhard BM. ACS Applied Materials and Interfaces. 2010; 2:35–40. [PubMed: 20161660]
- 51. van Manen H-J, Verkuiljen P, Wittendorp P, Subramaniam V, van den Berg TK, Roos D, Otto C. Biophysical Journal. 2008; 94:L67–L69. [PubMed: 18223002]
- 52. Chung I, Akita R, Vandlen R, Toomre D, Schlessinger J, Mellman I. Nature. 2010; 464:783–787. [PubMed: 20208517]

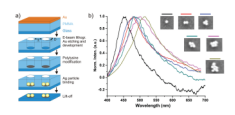


Figure 1.

a) Process flow for template assisted fabrication of nanoparticle clusters. The intercluster separation (Λ) and cluster site binding diameter (D) are indicated. b) Scattering spectra for selected silver nanoparticle clusters of known size (n \leq 7) and geometry. The scattering spectra gradually red-shift and overall broaden with increasing cluster size. Based on the spectral position of the peak scattering resonances for small to mid-sized two-dimensional clusters, we anticipate that the spectral range 425 \sim 525 nm is most relevant for an optical sizing of nanoparticle clusters in this size range.

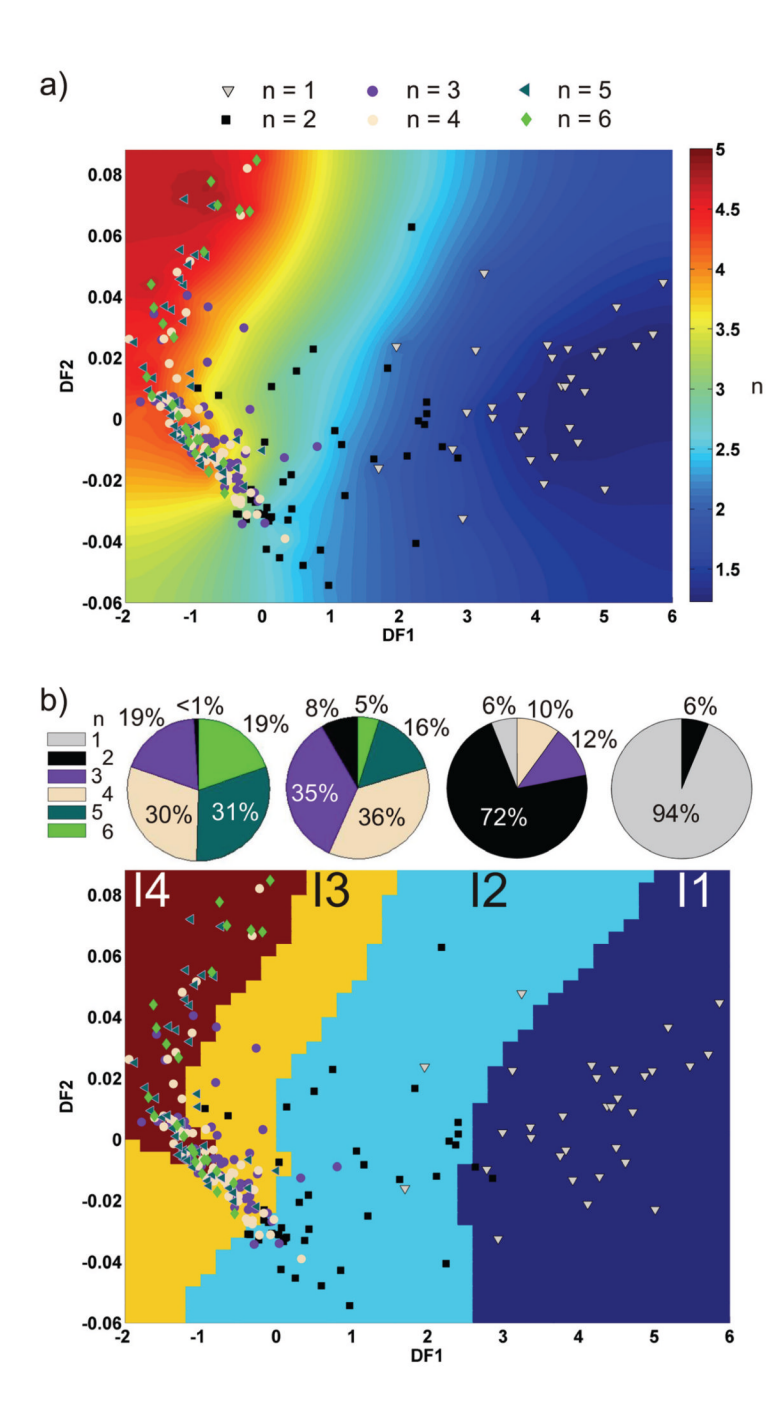


Figure 2. a) Score plot of silver nanoparticle clusters with sizes n=1-6 in the DF1–DF2 plane. The fitted cluster size surface as function of DF1 and DF2 is included as contour plot. b) Partition of the DF1–DF2 plane into four subspaces corresponding to cluster size contour intervals of n(I1) = [1-1.8,] (blue), n(I2) = [1.8-3.2] (turquoise), n(I3) = [3.2-4.1] (yellow), and n(I4) > 4.1 (brown). The cluster size composition for each interval (I1–I4) is presented as a pie chart.



Figure 3.

Results from an independent benchmark sizing experiment using random nanoparticle clusters. The association levels I1–I4 show nearly identical compositions as obtained with the training set confirming the reproducibility of the optical cluster sizing approach.

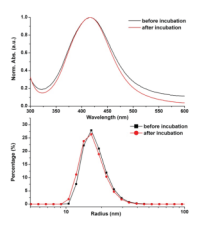


Figure 4.

a) UV-Vis spectra of silver immunolabels before (black) and after (red) incubation with A431 cells. b) Number distribution of the nanoparticle labels as determined through dynamic light scattering (DLS). Both the UV-Vis and DLS data show no systematic shift confirming that the nanoparticles are stable under the imaging conditions.

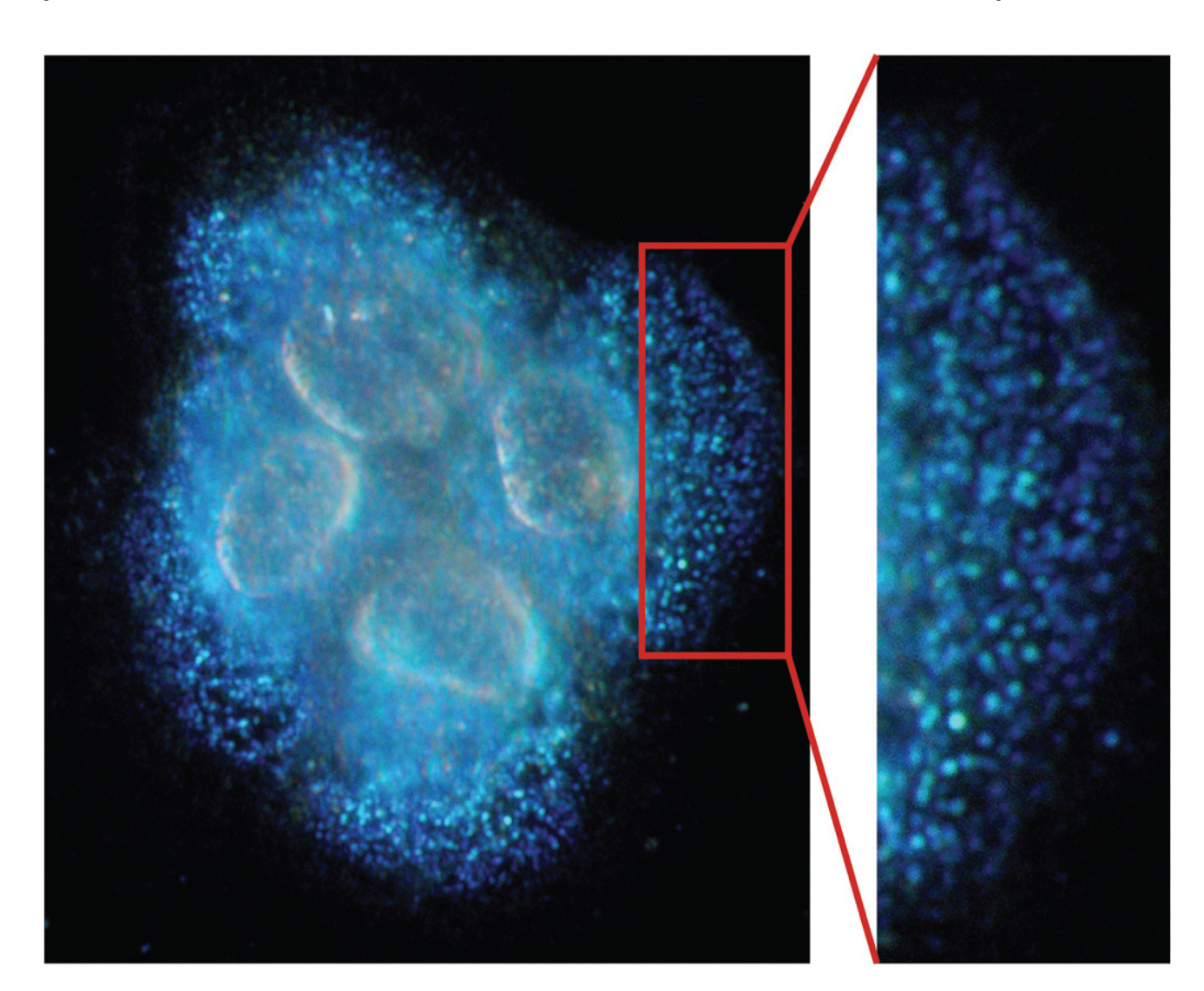


Figure 5.Darkfield image of A431 cells incubated with anti-EGFR functionalized silver nanoparticles. The different shades of blue dots of the silver immuolabels on the cell surface indicate different association levels.

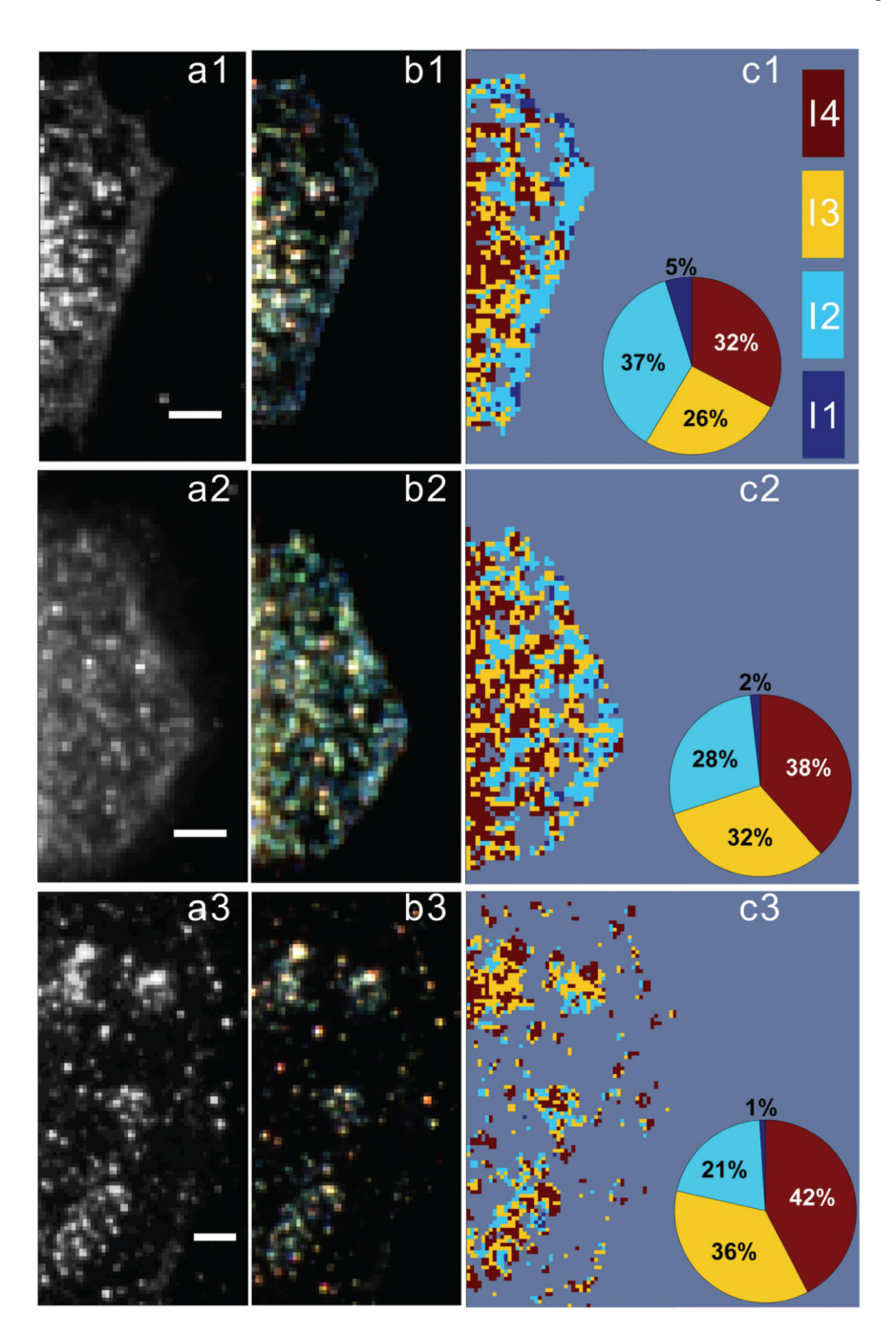


Figure 6. a1–3) Whitelight images of peripheral cell membrane regions of three different silver nanoparticle labeled A431 cells (1–3). All scale bars are 5 μ m. b1–3) Composite images showing the relative distribution of the scattered light on the monitored 510 and 494 nm (red), 473 and 445 (green) and 427 nm (blue) color channels. c1–3) Spatial maps of the nanoparticle association levels I1–I4. A break-down of the integrated contributions from the individual nanoparticle association levels is included as pie chart for each cell.